

Received August 18, 2017, accepted October 7, 2017, date of publication January 1, 2018, date of current version February 28, 2018.

Digital Object Identifier 10.1109/ACCESS.2017.2788942

Automatic LPI Radar Waveform Recognition Using CNN

SEUNG-HYUN KONG[✉], (Senior Member, IEEE), MINJUN KIM, LINH MANH HOANG, AND EUNHUI KIM

The CCS Graduate School of Green Transportation, Korea Advanced Institute of Science and Technology, Daejeon 34141, South Korea

Seung-Hyun Kong and Minjun Kim are co-first authors.

Corresponding author: Seung-Hyun Kong (skong@kaist.ac.kr)

The authors gratefully acknowledge the support from Electronic Warfare Research Center at Gwangju Institute of Science and Technology (GIST), originally funded by Defense Acquisition Program Administration (DAPA) and Agency for Defense Development (ADD).

ABSTRACT Detecting and classifying the modulation scheme of the intercepted noisy low probability of intercept (LPI) radar signals in real time is a necessary survival technique required in the electronic warfare systems. Therefore, LPI radar waveform recognition technique (LWRT) has gained an increasing attention recently. In this paper, we propose a convolutional neural network (CNN)-based LWRT, where the input and hyperparameters of the CNN, such as the input size, number of filters, filter size, and number of neurons are designed based on various signal conditions to guarantee the maximum classification performance. In addition, we propose a sample averaging technique to efficiently reduce the large computational cost required when the intercept receiver needs to process a large amount of signal samples to improve the detection sensitivity. We demonstrate the performance of the proposed LWRT with numerous Monte Carlo simulations based on the simulation conditions used in the recent LWRTs introduced in the literature. It is testified that the proposed LWRT offers significant improvement, such as robustness to noise and recognition accuracy, over the recent LWRTs.

INDEX TERMS Convolutional neural network, low probability of intercept, radar waveform recognition.

I. INTRODUCTION

Fast and efficient low probability of intercept (LPI) radar waveform recognition is one of the core functions required in the electronic warfare (EW) systems, such as electronic support and electronic intelligence (ES/ELINT), electronic protection (EP), and electronic attack (EA) systems. In practice, automatic radar waveform recognition technique is a core survival technique for an intercept receiver performing threat recognition and radar emitter identification [1]. On the contrary, radar signals should be designed to have LPI properties [2] so that a radar signal is not easily detected and recognized by intercept receivers. Therefore, intercept receivers should be necessarily equipped with an automatic LPI radar waveform recognition function that has highly reliable detection, classification, and identification capabilities to recognize the presence of LPI radar signals in advance.

In the literature, there have been a few LPI waveform (i.e., LPI radar waveform) recognition techniques (LWRT) that utilize feature extraction techniques and classification techniques to extract features from the intercepted signal and to classify the intercepted signal based on the extracted features, respectively. For the feature extraction, there are time-frequency analysis (TFA) techniques using an individual

transform, such as short-time Fourier transform (STFT) [3], Wigner Ville Distribution (WVD) [2], [4], and Choi-William Distribution (CWD) [2], [5], [6], and there are TFA techniques utilizing a combination of two transforms, such as WVD with CWD [7], [8] and WVD with ambiguity function (AF) [9]. On the other hand, for the classification techniques, there are hierarchical decision tree (HDT) [3], [9] and artificial neural networks (ANN) based on multilayer perceptron (MLP) [2], [5], [7], recurrent neural networks (RNN) [8], and convolutional neural networks (CNN) [4], [6].

In [2] and [5], the time-frequency image (TFI) produced by a TFA technique is cropped and used as an input to an ANN based on MLP. The LWRTs in [7] and [8] extract various signal features from the complex envelope (CE) of the intercepted signal, such as the second order statistics and instantaneous frequency and phase, and also extract TFI features of the intercepted signal. The signal features and the TFI features are then used as an input to an ANN based on MLP [7] or based on RNN [8]. The LWRTs in [3] and [9] introduce classification techniques based on the HDT, where the signal features obtained using TFA techniques are compared to the thresholds to identify the correct branch in the decision tree. These classification techniques based on the

HDT can achieve a fast classification performance, however, the binary (i.e., yes or no) decisions made by comparing a feature value against a threshold may have performance degradation when a decision needs to consider multiple features at the same time. Note that the LWRTs [3], [7]–[9] exclude all of the four polytime codes introduced in [2] as representative LPI waveform modulations, and signal features to distinguish polytime codes are not studied. In addition, the performance of LWRTs [7], [8] degrades significantly in the presence of carrier frequency estimation error (CFEE), since the calculated signal features from the CE can be corrupted by the remaining frequency component. In fact, the LWRT in [8] assumes that there is no remaining frequency component (i.e., zero center frequency) in the CE, however, Lundén and Koivunen [7] show that there is about 20% (or larger) performance degradation for LPI signals with SNR of -3dB (or less) in the presence of CFEE.

The recent LWRT in [6] utilizes CWD to generate TFI and uses the binary version of the generated TFI for an input to the CNN based classification technique. This technique has robustness against the CFEE, since the effect of CFEE on the TFI is merely an offset in the object image location and the CNN is generally robust to the changes in the image topology [10]. The performance of [6] shows a strong improvement compared to the conventional techniques in distinguishing a set of LPI radar waveforms including the four polytime codes [2] at SNR of -4dB or higher. However, the technique [6] does not consider four polyphase codes (e.g., P1, P2, P3, and P4) other than the Frank code. In addition, the LWRT in [6] assumes that the Barker code based BPSK (binary phase shift keying) waveform is repeating multiple times during the pulse interval so that the collected signal samples of the BPSK waveform are from consecutive multiple code periods, while other waveforms (i.e., except the BPSK) are collected for a single period. This assumption makes the Barker modulated signal object in the TFI be very different from that of the T1 code (a polytime code), and otherwise, the TFI of the two codes (i.e., BPSK and T1) may have a similar shape especially in the presence of large noise. In addition, the input format (i.e., binary images) and hyper-parameters (i.e., the parameters that define the CNN in detail such as input size, filter size, and number of filters) of the CNN in [6] are identically the same to those of [11] that is originally developed for hand-writing digit recognition, and the modification is only made to the fully connected (FC) layer by adjusting the number of neurons (i.e., nodes) according to the empirical formula [12]. In practice, larger TFI input size and amplitude (i.e., intensity) information of the objects in the TFI can be better to the CNN, when the objects have subtle differences that are better observed with finer image resolution and amplitude information. In practice, the hyper-parameters of CNN should be designed and verified to maximize the recognition performance with various simulations.

In fact, most of the studies [2], [6]–[8] in the field exploit less than two thousand signal samples and show a severe performance degradation as the SNR of the intercepted signal

decreases below -4dB . To overcome this limit, Kishore and Rao [9] utilize a much larger number of signal samples, (e.g., 10^4 samples) to increase the processing gain (PG) and utilize fractional Fourier transform (FRT) to reduce the computational cost required for the employed TFA techniques such as Radon ambiguity transform (RAT) and Radon-WVD (RWT). As a result, the LWRT in [9] can classify LPI radar waveforms at the SNR of -10dB .

In this paper, we propose an LWRT based on CNN, where the considered LPI waveforms are all of the twelve pulse compression waveforms defined in [2] which includes all of the five polyphase and four polytime codes. In addition, all of the waveforms are collected only for a single period, and the input to the CNN is a grayscale TFI (i.e., with amplitude information). The hyper-parameters of the proposed CNN are designed with various simulations and verified to guarantee the maximum performance. In addition, we exploit the sample averaging technique (SAT), used for fast and high sensitivity GPS acquisition, in order to process a large number of signal samples with reduced computational cost effectively. The performance of the proposed LWRT is compared to the recent LWRTs in [6], [8], and [9] for the signal parameters and simulation conditions used in the studies [6], [8], [9]. The proposed technique without the SAT shows significant performance improvement over the recent LWRTs in [2] and [6]–[8], and the proposed technique with the SAT has much better performance than [9] in terms of both the sensitivity and classification accuracy for the same number of signal samples. The superior performance of the proposed technique is demonstrated with numerous Monte Carlo simulations for a wide range of SNR of all waveforms.

This paper is organized as follows. Section II presents the proposed LWRT and describes the LPI radar waveforms considered in this paper. Section III introduces the proposed pre-processing technique (i.e., the SAT), the TFA technique (i.e., CWD) used to generate TFI input to the CNN, and the waveform patterns of the twelve LPI waveforms on the resulting TFIs. The TFI resizing process is also described in Section III. The CNN input size and the hyper-parameters are analyzed and determined in Section IV, and the performance of the proposed technique is compared to the recent LWRTs in Section V. Finally, the conclusion of this paper is drawn in Section VI.

II. SYSTEM AND WAVEFORMS

In this section, we present the system structure of the proposed LWRT and the definition of the twelve LPI radar waveforms considered in this paper.

A. PROPOSED LWRT

Fig.1 illustrates the block diagram of the proposed LWRT. The intercepted signal is down-converted to an intermediate frequency (IF) f_I and then sampled at $f_s = (1/T_s)$ to yield $y[k]$, where k is the sample index. A set of consecutive N signal samples collected over τ_{pw} seconds (i.e. $N = \tau_{pw} \cdot f_s$) is fed into the preprocessing-I block for the proposed SAT. Similar to [6]–[9], this paper focuses on classifying LPI radar

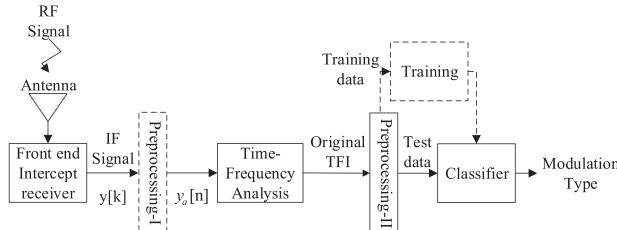


FIGURE 1. Proposed LPI radar waveform recognition system.

waveforms and assumes that the signal samples are collected for a signal pulse interval (τ_{pw}) and the coarse estimate of the carrier frequency is obtained. Note that the preprocessing-I block is an optional function used only when $f_s/(f_I + B_s/2)$ is by multiple times larger than N_{sc} that is the required number of samples per cycle of a carrier wave of the highest frequency allowed by the receiver bandwidth B_s . Note that $N_{sc} \geq 4$ does not cause an SNR loss larger than 1.0dB. The details of the proposed preprocessing-I are discussed in Section III. As shown, depending on the use of the SAT in the preprocessing-I, the input to the TFA block can be either $y[k]$ (when the SAT is not used) or $y_a[n]$ (when the SAT is used). In the TFA block, the signals are zero-padded to make input size of 2048 samples to the CWD for FFT operation. The TFI is then pre-processed in the preprocessing-II block to resize the TFI to the required input size for the proposed classification technique (i.e., CNN). For the training of the proposed LWRT, we generate training data set (the output of the preprocessing-II block) to train the CNN in off-line. The training phase of the system is depicted by the dashed arrows in Fig. 1. When the CNN is trained enough, LPI radar signals are classified in the test phase.

B. LPI RADAR SIGNALS

In this subsection, we define the twelve LPI radar waveforms [2], [13] considered in this paper. There are LFM, Costas code, BPSK, five polyphase codes (such as Frank, P1, P2, P3, and P4 codes), and four polytime codes (such as T1, T2, T3, and T4 codes) introduced in [2]. Note that the recent LWRTs introduced in the literature seldom considers all of the twelve waveform modulation schemes after [2] in 2004. For example, the studies in [7] and [8] consider LFM, Costas code, BPSK, and five polyphase codes, the study in [9] considers no modulation case, LFM, BFSK, and five polyphase codes, and the study in [6] considers LFM, Costas code, BPSK, and Frank code, and four polytime codes, which limits the application of the recent LWRTs.

When the SNR of the intercepted LPI signal is high enough, each LPI radar waveform shows a distinguishable pattern in the TFI produced by CWD (i.e., CWD-TFI). Therefore, it is useful to distinguish the waveform patterns using the CWD-TFI, which is discussed in detail in Section III. We also introduce the mathematical definition of the twelve LPI radar waveforms in this subsection.

In general, the discrete-time complex samples $y[k]$ can be expressed as

$$y[k] = x[k] + w[k] = a[k]e^{j\theta[k]} + w[k], \quad (1)$$

where $x[k]$ represents the down-converted (to f_I) discrete-time complex LPI radar signal samples, $w[k]$ is the complex additive Gaussian white noise (AGWN) process with two-sided power spectral density $N_0/2$, k is the sample index increasing every T_s for a sampling frequency f_s , $a[k]$ is the non-zero constant signal envelope (i.e., amplitude) within the pulse interval τ_{pw} such that $a[k] = A$ for $0 \leq kT_s < \tau_{pw}$, and $\theta[k]$ is the instantaneous phase of the LPI radar signal. Similar to [6], [8], and [9], we assume that the pulse period $\tau_{pp} = 1/f_{pp}$ is larger than τ_{pw} , where f_{pp} is the pulse repetition frequency, so that the duty cycle $DC = (\tau_{pw}/\tau_{pp})$ is assumed to be much smaller than 1. The instantaneous frequency $f[k]$ and the phase offset $\phi[k]$ as

$$\theta[k] = 2\pi f[k](kT_s) + \phi[k]. \quad (2)$$

In practice, there are two most common pulse compression techniques that categorize the twelve LPI radar waveforms considered in this paper into FM (Frequency Modulation) and PM (Phase Modulation) [14]. The instantaneous frequency $f[k]$ varies while the phase offset $\phi[k]$ is kept constant in the FM, and $f[k]$ is kept constant while $\phi[k]$ varies accordingly in the PM [2], [13], as defined in Table 1, where a subcode represents a partial pulse interval, within which $\phi[k]$ is fixed to a constant.

TABLE 1. Twelve LPI radar waveforms.

Modulation type	$f[k][Hz]$	$\phi_{i,j}[k][rad]$ for subcode
LFM	$\frac{f_0 + B}{\tau_{pw}}(kT_s)$	constant
Costas	f_j	constant
BPSK	constant	0 or π
Frank	constant	$\frac{2\pi}{M}(i-1)(j-1)$
P1	constant	$-\frac{\pi}{M}[(M-(2j-1))][(j-1)M+(i-1)]$
P2	constant	$-\frac{\pi}{2M}[2i-1-M][2j-1-M]$
P3	constant	$\frac{\pi}{\rho}(i-1)^2$
P4	constant	$\frac{\pi}{\rho}(i-1)^2 - \pi(i-1)$
T1	constant	$\text{mod}\left\{\frac{2\pi}{N_{ps}}\left[(N_g(kT_s) - j\tau_{pw})\frac{jN_{ps}}{\tau_{pw}}\right], 2\pi\right\}$
T2	constant	$\text{mod}\left\{\frac{2\pi}{N_{ps}}\left[(N_g(kT_s) - j\tau_{pw})\left(\frac{2j-N_g+1}{\tau_{pw}}\right)\frac{N_{ps}}{2}\right], 2\pi\right\}$
T3	constant	$\text{mod}\left\{\frac{2\pi}{N_{ps}}\left[\frac{N_{ps}B(kT_s)^2}{2\tau_{pw}}\right], 2\pi\right\}$
T4	constant	$\text{mod}\left\{\frac{2\pi}{N_{ps}}\left[\frac{N_{ps}B(kT_s)^2}{2\tau_{pw}} - \frac{N_{ps}B(kT_s)}{2}\right], 2\pi\right\}$

$\text{mod}\{a, b\}$: remainder after division between a and b

$\lfloor a \rfloor$: biggest integer smaller than or equal to a

III. PROPOSED PREPROCESSING TECHNIQUES

A. PREPROCESSING-I: SAMPLE AVERAGING TECHNIQUE (SAT)

When the intercept receiver needs higher detection sensitivity, the receiver may need to increase the processing

gain (PG) by increasing the sampling frequency f_s by multiple times than the sampling frequency required by the maximum observable frequency f_{\max} of the receiver, where

$$f_{\max} = f_I + B_s/2, \quad (3)$$

where B_s is the bandwidth of the receiver bandpass filter and is larger than the bandwidth of the signal B . However, as the size of signal samples increases, the computational cost for the TFA technique (i.e., CWD) increases exponentially, and the real-time detection of LPI radar signal may become difficult. The purpose of using the SAT is to reduce the computational cost required for the TFA block computing CWD by reducing the number of signal samples with at most a slight loss of SNR. The goal is achieved by producing averaged signal samples $y_a[n]$ which is the average (or coherent sum) of N_a consecutive signal samples $y[k]$ as

$$y_a[n] = \frac{1}{N_a} \sum_{k=0}^{N_a-1} y[k + nN_a], \quad (4)$$

where $N_a = N_1/N_{sc}$ and $N_1 = f_s/f_{\max}$ is the number of samples per carrier (wave) cycle for the maximum frequency f_{\max} allowed by the receiver bandpass filter. Note that $y_a[n]$ becomes the input to the TFA block in Fig. 1 when the SAT is used, but, otherwise, $y[k]$ becomes the input to the TFA block. In practice, the SAT is efficient, when N_{sc} and N_a are sufficiently large so that the phase difference between neighboring samples of $y[k]$ is negligible and the neighboring samples can be added (or averaged) coherently with a slight loss of SNR (e.g., much less than 1.0dB).

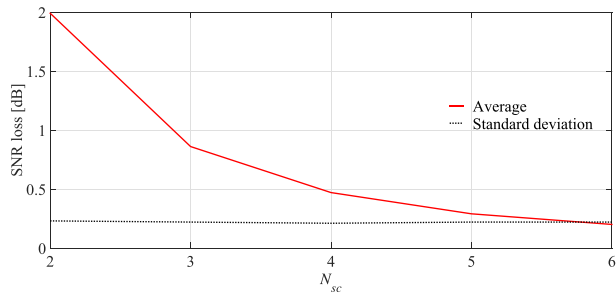


FIGURE 2. SNR loss with respect to N_{sc} .

Fig. 2 shows the relationship between N_{sc} and the mean SNR loss due to the SAT. As shown, N_{sc} of 4 or larger is required to have SNR loss less than 1.0dB in practice. Fig. 3(a), 3(b), and 3(c) highlight the signal power spectrum of a weak BPSK modulated LPI radar signal in the CWD-TFIs from $y[k]$ for an SNR of -8dB , from $y_a[n]$ for an SNR of -8dB , $N_a = 4$, and $N_{sc} = 4$, and from $y[k]$ for an SNR of -2dB , respectively, for an example. As shown, the signal power spectrum in Fig. 3(a) is much improved in Fig. 3(b), and the signal quality shown in Fig. 3(b) is similar to that in Fig. 3(c). In fact, the SNR values measured at the maximum signal power to the mean noise floor in Fig. 3(a), 3(b) and Fig. 3(c) are 15.22dB , 20.73dB and 21.37dB , respectively, which shows that the SNR degradation

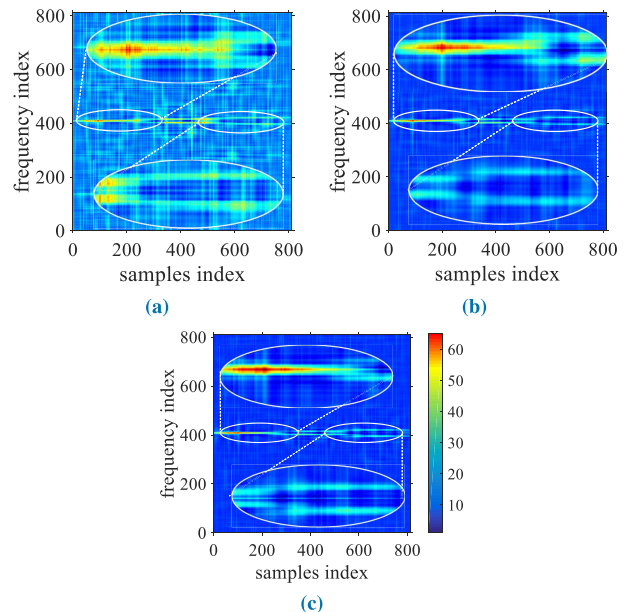


FIGURE 3. CWD-TFIs of a BPSK signal with and without the SAT. (a) CWD-TFI for $y[k]$ at $\text{SNR} = -8\text{dB}$, (b) CWD-TFI for $y_a[n]$ at $\text{SNR} = -8\text{dB}$, $N_a = N_{sc} = 4$, (c) CWD-TFI for $y[k]$ at $\text{SNR} = -2\text{dB}$.

is negligible with the proposed SAT. Therefore, as shown in Fig. 2 and Fig. 3, the use of the SAT does not distort the signal component in the CWD-TFI, while, the reduction of both the computational cost for the CWD and the SNR improvement are significant. In general, the CWD processing requires $\mathcal{O}(N^3 \log_2 N)$ complex multiplications, which means we can reduce the size of the computational cost for the CWD by $\mathcal{O}(N_a^3 \log_2 N / (\log_2 N - \log_2 N_a))$ times using the proposed SAT.

Note that the concept of the SAT is already used in the acquisition of GPS signals with unknown Doppler frequency. In [15] and [16], sample averaging is used when the obtained number of samples per a GPS chip is multiple times larger than 2. Since the consecutive samples being averaged can be from two neighboring GPS chips that may have opposite polarities, the averaging process can be destructive when, for example, the resulting averaged sample may be zero when a half of the original samples is from a $+1$ chip and the other half is from a -1 chip. Therefore, in [15], the sample averaging is performed for each possible sample offset and includes another process to find the sample offset that leads to the highest post-correlation SNR. However, exploiting the SAT to reduce the LPI radar signal sample size is different from GPS. For example, while a code chip has a very short time interval (almost a micro-second) and the unknown frequency is small in GPS, a subcode that may cause destructive averaging has a relatively very long interval but the unknown frequency can be larger than GPS in the LPI radar waveform with pulse compression. This is the reason for limiting N_a to maintain at least N_{sc} averaged samples per a carrier cycle at the highest allowed frequency (i.e., $f_I + B_s/2$) by the intercept receiver.

B. TFA TECHNIQUE FOR CWD-TFI

This subsection provides the essential description of the CWD used to produce the TFI of the intercepted signal in the TFA block and discusses the unique patterns of the twelve LPI waveforms based on their CWD-TFIs.

The CWD is based on the time-frequency distribution of cohen's class [13] with an exponential distribution (ED) kernel [17] as

$$\text{ED}_y(\ell, \omega) = 2 \sum_{\tau=-\infty}^{\infty} e^{-\alpha 2\omega\tau} \left[\sum_{\mu=-\infty}^{\infty} \frac{1}{\sqrt{4\pi\tau^2/\sigma}} e^{-\frac{(\mu-\ell)^2}{4\tau^2/\sigma}} \times y(\mu + \tau)y(\mu - \tau) \right], \quad (5)$$

where $\alpha = \sqrt{-1}$ is the imaginary unit, ℓ and ω are the time and angular frequency index variables, respectively, τ and μ are discrete variables, and ξ and ω are continuous variables. Note that the exponential kernel function $\varphi(\xi, \tau) = e^{-\xi^2\tau^2/\sigma}$ has a scaling factor σ that is an effective parameter for low pass filtering in the ambiguity function (AF) of the cohen's class. Since the CWD is generated from the AF using the kernel function and the 2-dimensional (2D) Fourier transform, the CWD of the intercepted signal $y[k]$ comprised of multiple frequency components has high power spectrum intensity near the center frequency and some power spectrum components away from the center frequency due to the auto-terms and (non-zero frequency) cross-terms in the AF, respectively [18]. The scaling factor σ in (5) can be used to lessen the cross-terms in the CWD, while the frequency resolution in the CWD is degraded. In the proposed technique, we use $\sigma = 1$ as a balance between the cross-terms suppression and the frequency resolution of the auto-terms in the resulting CWD-TFI.

In addition, we can limit the summations over τ and μ in (5) by applying rectangular windows (RW) $W_P(\tau)$ and $W_Q(\mu)$, respectively, to the ED kernel, and we exploit $\omega = 2k/N$ to modify (5) into a form of Fast Fourier Transform (FFT) as

$$\text{RWED}_y(\ell, k) = 2 \sum_{\tau=-\infty}^{\infty} W_P(\tau) e^{-\alpha 2k\tau/N} \times \left[\sum_{\mu=-\infty}^{\infty} W_Q(\mu) \frac{1}{\sqrt{4\pi\tau^2/\sigma}} e^{-\frac{\mu^2}{4\tau^2/\sigma}} \times y(\ell + \mu + \tau)y(\ell + \mu - \tau) \right], \quad (6)$$

where $W_P(\tau)$ and $W_Q(\mu)$ are the rectangular windows of unit amplitude for $-P/2 \leq \tau \leq P/2$ and $-Q/2 \leq \mu \leq Q/2$, respectively. In the following, we discuss the unique patterns of the twelve LPI waveforms based on their CWD-TFI shown in Fig. 4.

1) LINEAR FREQUENCY MODULATION (LFM)

There are two kinds of LFM [13] schemes; monotonous frequency modulation, where $f[k]$ increases or decreases from

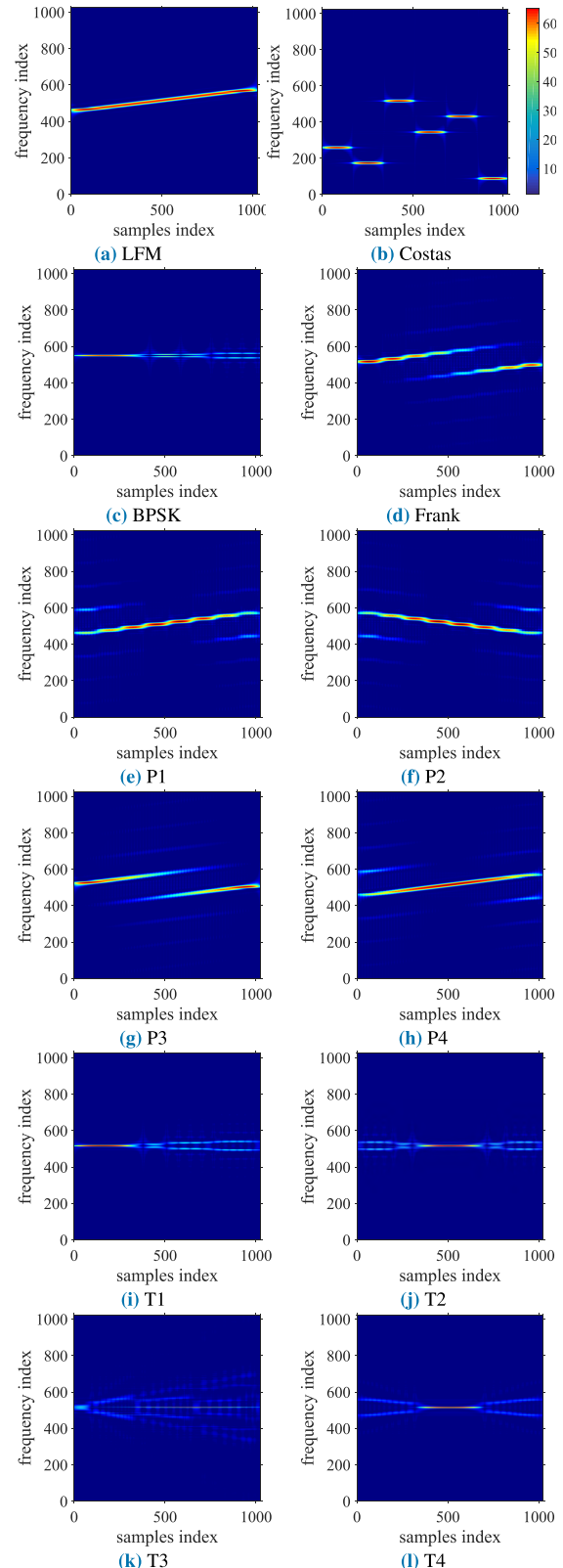


FIGURE 4. CWD-TFIs of the 12 LPI radar waveforms considered in this paper for SNR = 10dB. (a) LFM. (b) Costas. (c) BPSK. (d) Frank. (e) P1. (f) P2. (g) P3. (h) P4. (i) T1. (j) T2. (k) T3. (l) T4.

an initial frequency f_0 to $f_0 \pm B$ linearly within the pulse interval τ_{pw} , and triangular frequency modulation, where $f[k]$

increases from f_0 to $f_0 + B$ and decreases back to f_0 at the end of τ_{pw} . Since the LFM radar signal has its power spectrum spread over the signal bandwidth B as shown in Fig. 4(a), the signal is good for an LPI radar waveform.

2) FREQUENCY SHIFT KEYING (FSK)

In FSK, $f[k] = f_j$ follows the frequency hopping (FH) sequence $[f_1, f_2, \dots, f_{N_F}]$, where N_F is the number of FH sequence. In general, FSK modulated radar signal has LPI property because of the pseudo-random frequency hopping pattern over a wide signal bandwidth B . In this paper, we use the Costas code for a FH sequence [13], and its CWD-TFI is shown in Fig. 4(b).

3) BINARY PHASE SHIFT KEYING (BPSK)

BPSK modulation is a PM, where the phase offset $\phi[k]$ has only 2 states (i.e., 0 and π) as shown in Table 1. In BPSK, the sidelobe level in the autocorrelation result is not larger than $1/\rho$ of the main lobe, where the length of the sequence is ρ . This characteristic provides an advantage to cope with the target masking problem [13], but BPSK modulated signals can be easily detected due to the simple modulation, so it is not used for an LPI radar waveform modulation [2] in practice. However, its CWD-TFI in Fig. 4(c) has a noticeable similarity to the CWD-TFI of the T1 code as shown in Fig. 4(i). Therefore, we include the BPSK modulation for a performance comparison as it is included in the recent studies [6], [8], [9].

4) POLYPHASE

Polyphase modulation is a PM, where the phase offset $\phi[k]$ has more than 2 states. This characteristics is useful for an LPI radar signal and provides a low sidelobe level in the auto-correlation result. The CWD-TFIs for the polyphase codes (i.e., Frank, P1, P2, P3, and P4 codes) are shown in Fig. 4(d)-4(h), respectively. Among the polyphase, Frank, P1, and P2 codes are derived from step approximations to the LFM signal and P3 and P4 codes are from linear approximations to the LFM signal [2]. Due to the difference in the approximations to the LFM signal, the frequency variation of the Frank, P1, and P2 codes has staircase patterns in the CWD-TFIs, whereas P3 and P4 codes have linear frequency variation, as shown in Fig. 4(d)-4(h). However, the big jump in the middle of the Fig. 4(d) and 4(g), separating the power spectrum into two distinctive components with weaker amplitude (intensity) than the intensities at both ends (i.e., the beginning and the end), is because the Frank and P3 codes have the largest phase increments between subcodes in the middle of the code. On the contrary, P1, P2, and P4 codes have the largest phase increments at both ends of the codes, which results in its power spectrum separation and weaker intensities at both ends of the code and higher intensity in the middle of the code. Note that P1 and P2 codes have multiple similarities as shown in Fig. 4(e) and 4(f), respectively, in that there are staircase patterns and the power spectrum is concentrated in the middle of the code, and the only difference is the opposite slope. Note also that while both

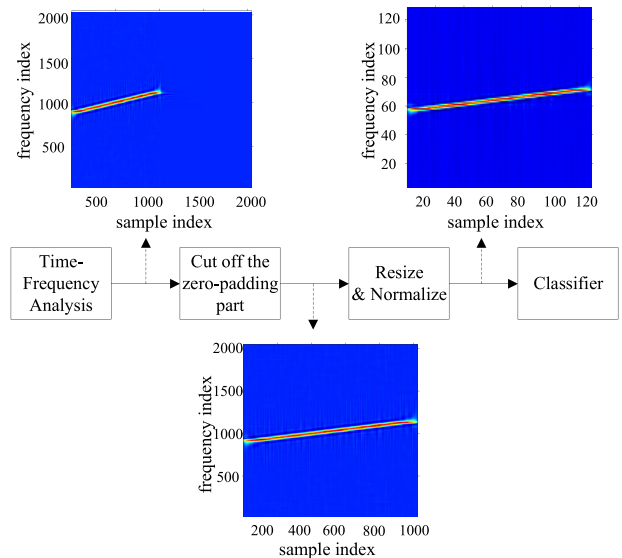


FIGURE 5. Preprocessing-II for cropping and resizing.

of the LFM and P4 codes have linearly increasing frequency patterns, the LFM has a uniform power spectrum distribution over the signal bandwidth, but the P4 code has its power spectrum concentrated (i.e., higher intensity) in the middle of the code. The power spectrum separation at both ends of the P4 code may not distinctive when the signal is corrupted by large noise.

5) POLYTIME

Polytime modulation is another PM, where the phase offset $\phi[k]$ is quantized into a user-selected number of states (N_{ps}) and user-selected number of segment (N_g). In this paper, we consider two states (i.e., 0 and π) for the phase offset $\phi[k]$, which is the most popular and applicable case, because of the simplicity in generating the waveforms [2], [19]. Among the polytime modulations, T1 and T3 codes have $\phi[k] = 0$ at the beginning and $\phi[k] = 0$ or π in the middle and at the end of the code. Due to this fact, T1 and T3 codes have constant frequency at the beginning and symmetrical power spectrum distribution across the center frequency in the middle and at the end of the code. As a result, the CWD-TFIs of T1 and T3 codes have ‘<’ shapes, as shown in Fig. 4(i) and 4(k). On the other hand, T2 and T4 codes have $\phi[k] = 0$ at the center of the code and $\phi[k] = 0$ or π at both ends of the code, which result in ‘X’ shapes in the CWD-TFIs as shown in Fig. 4(j) and 4(l). Note that the CWD-TFIs for BPSK and T1 shown in Fig. 4(c) and Fig. 4(i), respectively, are similar and can be difficult to distinguish when the power spectrum in the tail (i.e., samples with indices larger than 500) are buried under a strong noise (i.e., low SNR cases). Similarly, T2 and T4 codes shown in Fig. 4(j) and 4(l), respectively, can be difficult to distinguish when the power spectrum at the both sides (i.e., samples with indices less than 300 and those larger than 700) are buried under a strong noise (i.e., low SNR cases).

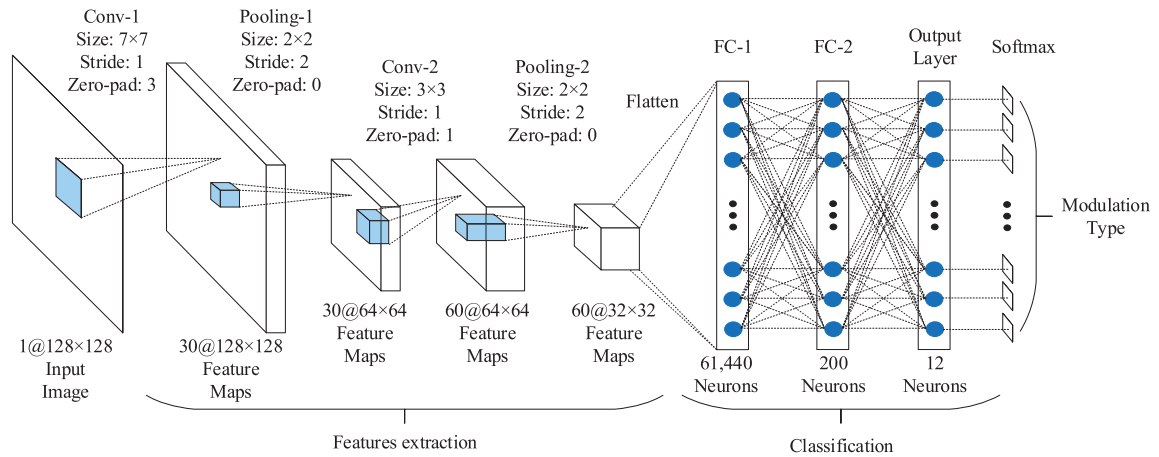


FIGURE 6. The CNN structure for the classification technique.

C. PREPROCESSING-II: IMAGE RESIZING

Studies in [7] and [8] apply noise filtering to the input image to lessen the effect of the noise and, thus, to improve SNR, but it may result in a loss of signal information contained in the details of the image. Therefore, preserving the details in the CWD-TFI (e.g., the staircase patterns in the Frank and P1 codes, weaker intensities at both ends of the P4, at the tail of BPSK and T1, and the sides of T2 and T4) is critical to the classification performance. Therefore, we use intact CWD-TFI for any level of the noisy signal in the proposed LWRT.

In the proposed LWRT, we collect signal samples of less than 2048 and zero-pad to make an input size of 2048 samples in order to use the FFT algorithm in the CWD. Then, we crop the CWD-TFI to remove the pixels in the CWD-TFI generated by the zero-padding. The cropped CWD-TFI is then resized to further reduce the input size appropriately to the CNN, which is to lessen the computational cost for CNN while guaranteeing good classification performance. However, we should not reduce the cropped CWD-TFI to a too small size, because the details of the object in the CWD-TFI can be lost, which may result in a significant performance degradation. Therefore, we need a balance between the computational cost and the classification performance in regard to the input size of the CNN. In the proposed LWRT, we use $P = Q = 2048$ for the rectangular window $W_P(\tau)$ and $W_Q(\mu)$ so that the produced CWD-TFI has 2048×2048 pixels, and we resize the TFI into 128×128 pixels using the nearest-neighbor interpolation (NNI) technique [20]. Note that the cubic interpolation (CI) technique [21] may be used in the image resizing, however, we do not use the CI technique, since each resulting pixel may be corrupted by multiple noisy pixels in the original image. The image cropping and resizing processes are illustrated in Fig. 5.

IV. DESIGN OF THE PROPOSED CNN

In general, CNN shows a superb performance in image classification problems such as handwriting recognition and

various object recognition including human faces, license plates, hand gesture, logos, and texts [22]. This is the reason we employ the CNN in the proposed LWRT, and this section introduces the design of the proposed CNN based classification technique.

As shown in Fig. 6, CNN consists of a (image) feature extraction block and a classification block. Because the feature extraction block is integrated inside, CNN does not require any prior feature extraction function [11]. In addition, the convolution and pooling processes in the CNN make the CNN robust to the geometrical distortions, such as scaling, shift, and rotation, and to the noise in the input image [11].

Considering the number of classes to classify, the fact that the input image is in a gray scale, and the subtle shapes of the image objects of the twelve LPI radar waveforms in the CWD-TFIs, we can observe that there are multiple similarities between the hand-writing recognition problem [11] and the problem considered in this paper. Therefore, we start with the basic structure of the CNN studied in [11] and [23]–[25] to develop an appropriate CNN structure for the proposed LWRT. The basic structure of the CNN can be described in a sequence of functions as Input – Conv – ReLU – Pooling – Conv – ReLU – Pooling – FC – Dropout – FC, where Conv represents the convolution layer, ReLU is the rectified linear unit, Pooling is the pooling layer, FC denotes the full-connected layer, and Dropout is the dropout layer. Based on the basic structure, we design the hyper-parameters, such as the input size, convolution filter size, the number of Conv feature maps, and the number of neurons in the FC, to find the optimal structure for the LPI waveform classification problem based on numerous Monte Carlo simulations for various conditions.

Due to the large number of independent parameters to determine, we exploit the Conv filter size [5x5] made in [11], [23], and [24] for an initial choice. However, we use 400 as an initial value (large enough) for the number of neurons in the FC layer, which is different from the number

TABLE 2. Determination of the hyper-parameters of the CNN.

Input size	First Conv Filter number	Second Conv Filter number	First Conv Filter size	Second Conv Filter size	Number of neurons	Average pcc for SNR=−4, −6, −8dB
64×64	10	20	5×5	5×5	400	83.08
64×64	20	40	5×5	5×5	400	84.11
64×64	30	60	5×5	5×5	400	89.56
64×64	40	80	5×5	5×5	400	86.83
128×128	10	20	5×5	5×5	400	89.64
128×128	20	40	5×5	5×5	400	87.86
128×128	30	60	5×5	5×5	400	90.08
128×128	40	80	5×5	5×5	400	89.19
256×256	10	20	5×5	5×5	400	88.22
256×256	20	40	5×5	5×5	400	88.72
256×256	30	60	5×5	5×5	400	87.72
256×256	40	80	5×5	5×5	400	87.47
128×128	30	60	3×3	3×3	400	88.78
			5×5	3×3	400	90.89
			5×5	5×5	400	90.08
			7×7	3×3	400	92.78
			7×7	5×5	400	88.86
			7×7	7×7	400	91.75
			9×9	3×3	400	91.89
			9×9	5×5	400	87.72
			9×9	7×7	400	91.94
			9×9	9×9	400	89.50
128×128	30	60	7×7	3×3	100	91.94
					200	93.67
					300	92.53
					400	92.78
					500	89.19
					600	90.72
					700	90.25

of neurons (i.e., 100 ~ 200) used in [11] and [23]–[25]. This initial choice of neurons is not only because the input CWD-TFI size is much larger than the image size used in [11] and [23]–[25], but also because of the high complexity of the image features of the twelve LPI radar waveforms shown in Fig. 4. However, due to a large number of neurons in the FC layer, we may have an overfitting problem, for which we employ a Dropout layer between the two FC layers denoted as FC-1 and FC-2 in Fig. 6.

In the first step of the design, we determine the input size of the CNN and the number of convolution filters with various simulations, where the input size is related to the resolution of the objects in the CWD-TFI, and the number of convolution filters is to find elementary visual features such as oriented edges, end-points, and corners. The visual features are then combined by the subsequent layers to detect higher-order features [11]. We develop multiple LWRTs shown in Fig. 1 for various input sizes to the CNN, such as [64×64], [128×128], and [256×256], and for various numbers of convolution filters used in the first/second convolutional layers, such as 10/20, 20/40, 30/60, and 40/80, and test the LWRTs for twelve LPI radar waveforms with low SNR, such as −4dB, −6dB, and −8dB. Note that the choice of the test SNR range is effective since the performance of the LWRTs starts to degrade for SNRs lower than −4dB and drops to a very low percentage of the correct classification (pcc) for SNRs lower than −8dB.

Table 2 shows some of the simulation results to testify the design of the proposed CNN. As shown, the input size of [128×128] and the numbers of convolution filters for the first and second layers equal to 30 and 60, respectively, produce the best result. In the next 10 rows (i.e., from the 13th row to the 22nd row) of the Table 2, we present the test results for various filter sizes of the first and the second convolutional layers, where it is assumed that the filter size of the first layer is larger or equal to that of the second layer [11], [25]. It turns out that the filter sizes of [7×7] and [3×3] for the two layers produce the best result. As for the stride size in the convolutional layers, since the CNN needs to extract features from the subtle shapes of the image objects, we select a unit stride size. For the determination of the hyper-parameters in the pooling layers, we use the max pooling [26] with 2×2 filter size, stride size 2, and no zero-padding, which are the common choice in [23] and [24]. Note also that in the nonlinear layer (omitted in Fig. 6 for illustrational simplicity), we use ReLU as a common choice. The last 7 rows of Table II shows that the performance of the LWRT is the best when there are 200 neurons in the FC-2. Note that there is a Dropout layer (of 50% rate) omitted in Fig. 6 for illustrational simplicity, between the FC-1 and FC-2 to avoid a possible overfitting problem [27]. The performance with and without the Dropout layer is 93.67% and 91.51%, respectively. The details of the final design of the CNN are described in Fig. 6.

V. PERFORMANCE DEMONSTRATION AND COMPARISON TO THE CONVENTIONAL TECHNIQUES

In this section, we compare the performance of the proposed LWRT to the recent LWRTs [6], [8], [9] introduced in the literature with numerous Monte Carlo simulations.

A. PERFORMANCE COMPARISON TO THE LWRT IN [9]

The first performance comparison is between the proposed LWRT with the SAT and the LWRT in [9] that utilizes FRT to reduce the computational cost for processing a large amount of signal samples. The waveform modulations considered are no modulation, BFSK, LFM, Frank, P1, P2, P3, and P4 codes, and the same simulation conditions including the number of signal samples in [9] are used in the simulations of the proposed LWRT with the SAT. Therefore, $N = 10,000$ samples are collected for each trial, and the tested SNR levels are from -10dB to 10dB . To apply the SAT, we use $N_a = 10$ which results in $N_{sc} \geq 4$ and the CWD-TFIs of the averaged signals are used in the testing phase. Table 3 shows the simulation result for $\text{SNR} = -10\text{dB}$, which is the same condition introduced in [9]. We observe that the proposed LWRT achieves perfect performance in classifying all of the eight waveform modulations, whereas the performance of the LWRT in [9], shown within parentheses, is 90% in average.

TABLE 3. Confusion matrix for a comparison to [9].

	No Mod	BFSK	LFM	Frank	P1	P2	P3	P4
No Mod	100 (95)	0 (0)	0 (5)	0 (0)	0 (0)	0 (0)	0 (0)	0 (0)
BFSK	0 (5)	100 (95)	0 (0)	0 (0)	0 (0)	0 (0)	0 (0)	0 (0)
LFM	0 (5)	0 (0)	100 (95)	0 (0)	0 (0)	0 (0)	0 (0)	0 (0)
Frank	0 (0)	0 (0)	0 (0)	100 (85)	0 (5)	0 (0)	0 (10)	0 (0)
P1	0 (0)	0 (0)	0 (0)	0 (5)	100 (85)	0 (0)	0 (0)	0 (10)
P2	0 (0)	0 (0)	0 (0)	0 (0)	0 (0)	100 (95)	0 (5)	0 (0)
P3	0 (0)	0 (0)	0 (0)	0 (10)	0 (0)	0 (0)	100 (85)	0 (5)
P4	0 (0)	0 (0)	0 (0)	0 (0)	0 (10)	0 (5)	0 (0)	100 (85)

B. COMPARISON WITH THE LWRT IN [8]

The second performance comparison is between the proposed LWRT without the SAT and the recent LWRT in [8]. The waveform modulation schemes considered in [8] are LFM, BPSK, Costas, Frank, P1, P2, P3, and P4 codes, and the same simulation conditions in [8] are used for the simulations of the proposed LWRT. Fig. 7 shows that the classification performance of the proposed LWRT is superior to the LWRT in [8] by about 3dB in overall.

C. COMPARISON WITH THE LWRT IN [6]

The third performance comparison is between the proposed LWRT without the SAT and the CNN-based LWRT in [6].

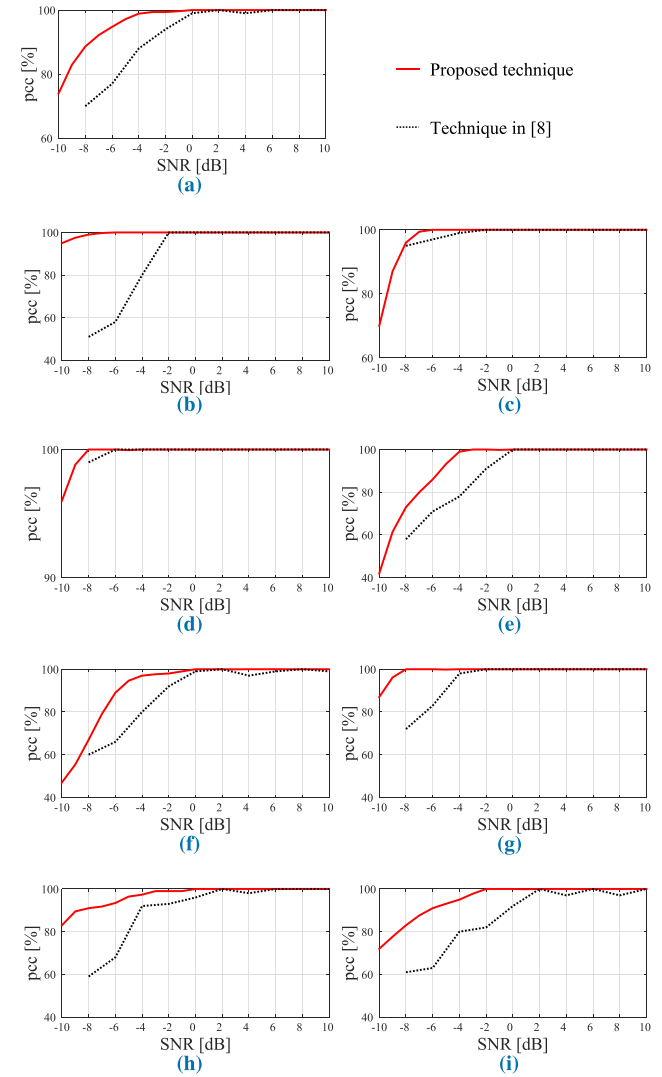


FIGURE 7. Comparison with the LWRT in [8]. (a) Overall. (b) LFM. (c) BPSK. (d) Costas. (e) Frank. (f) P1. (g) P2. (h) P3. (i) P4.

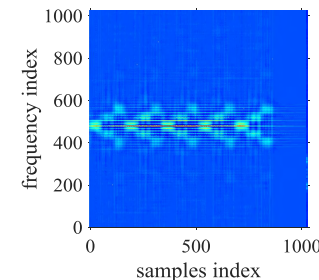


FIGURE 8. CWD-TFI of BPSK signals in [6].

The waveform modulation schemes considered in [6] are LFM, BPSK, Costas, Frank, T1, T2, T3, and T4 codes, and we use the same simulation conditions in [6] for the simulations of the proposed LWRT. However, there are two simulation conditions we do not follow [6]. Firstly, we do not assume that the BPSK waveform samples are obtained for multiple

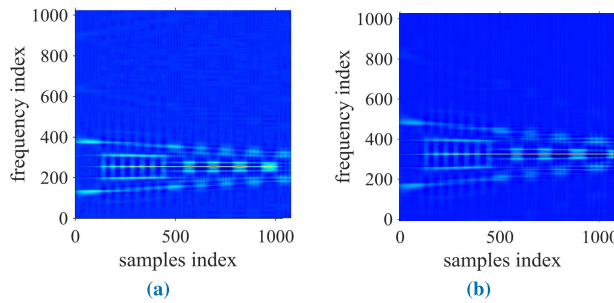


FIGURE 9. Incorrect CWD-TFIs of T4 code. (a) Copy of the CWD-TFI of T4 code in [6], (b) CWD-TFI of T4 code generated by the pseudo-code given in [2].

consecutive periods as assumed in [6]. Fig. 8 shows an example of a CWD-TFI of the BPSK waveform repeating 5 times. Therefore, the generated CWD-TFI of the BPSK waveform to test the proposed LWRT should be similar to the noise version of Fig. 4(c). Note that this condition for the proposed LWRT makes the classification more difficult, since the CWD-TFI of the repeating BPSK has a unique and distinctive shape when compared to other waveforms. Secondly, we do not agree with the CWD-TFI of T4 code shown in [6], which is copied in Fig. 9(a). In fact, the CWD-TFI of T4 code shown in Fig. 9(b), very similar to Fig. 9(a), is generated by using the pseudo-code given in the appendix of [2], where the phase offset follows

$$\phi[k] = \text{mod} \left\{ \frac{2\pi}{N_{ps}} \left\lfloor \frac{N_{ps}B(kT_s)^2}{2\tau_{pw}} - \frac{N_{ps}f_c(kT_s)}{2} \right\rfloor, 2\pi \right\}.$$

However, the correct formula for the phase offset of the T4 code is stated in Table 1, which is the exact mathematical definition in [2] and [14], and the CWD-TFI of T4 code should be as shown in Fig. 4(l). As a result, the correct CWD-TFI of T4 code can be confusing with that of T2 code shown in Fig. 4(j) in noisy conditions, but the shape of the incorrect CWD-TFI of the T4 code in Fig. 9(a) may be not easily confused with other LPI radar waveforms shown in Fig. 4

Fig. 10 shows the result of the proposed LWRT (without the SAT) compared to the result in [6], where the proposed LWRT has about 5dB improvement in overall. Notice that there is no result from [6] for SNR below -4dB . This significant improvement is because the proposed LWRT utilizes the grayscale input that has amplitude information preserved in the CWD-TFI, and the input size and the hyper-parameters of the CNN are designed to maximize the classification performance. These improvements also allow the proposed LWRT to classify a larger number of modulation schemes (i.e., 12 in total) as presented in the next subsection.

D. CLASSIFICATION PERFORMANCE OF THE PROPOSED LWRT FOR ALL OF THE TWELVE LPI RADAR WAVEFORMS

In addition to the performance comparison of the proposed LWRT to the recent LWRTs for a subset of LPI radar waveforms, we show the performance of the proposed LWRT with

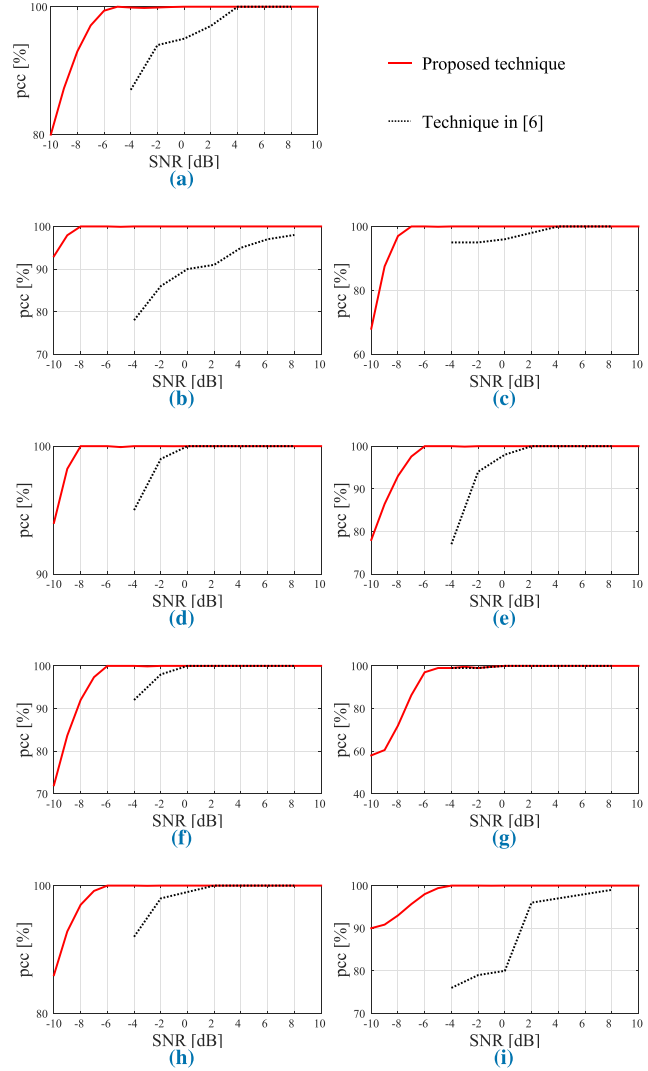


FIGURE 10. Comparison with the LWRT in [6]. (a) Overall. (b) LFM. (c) BPSK. (d) Costas. (e) Frank. (f) T1. (g) T2. (h) T3. (i) T4.

and without the SAT for all of the twelve waveforms [2] in this subsection.

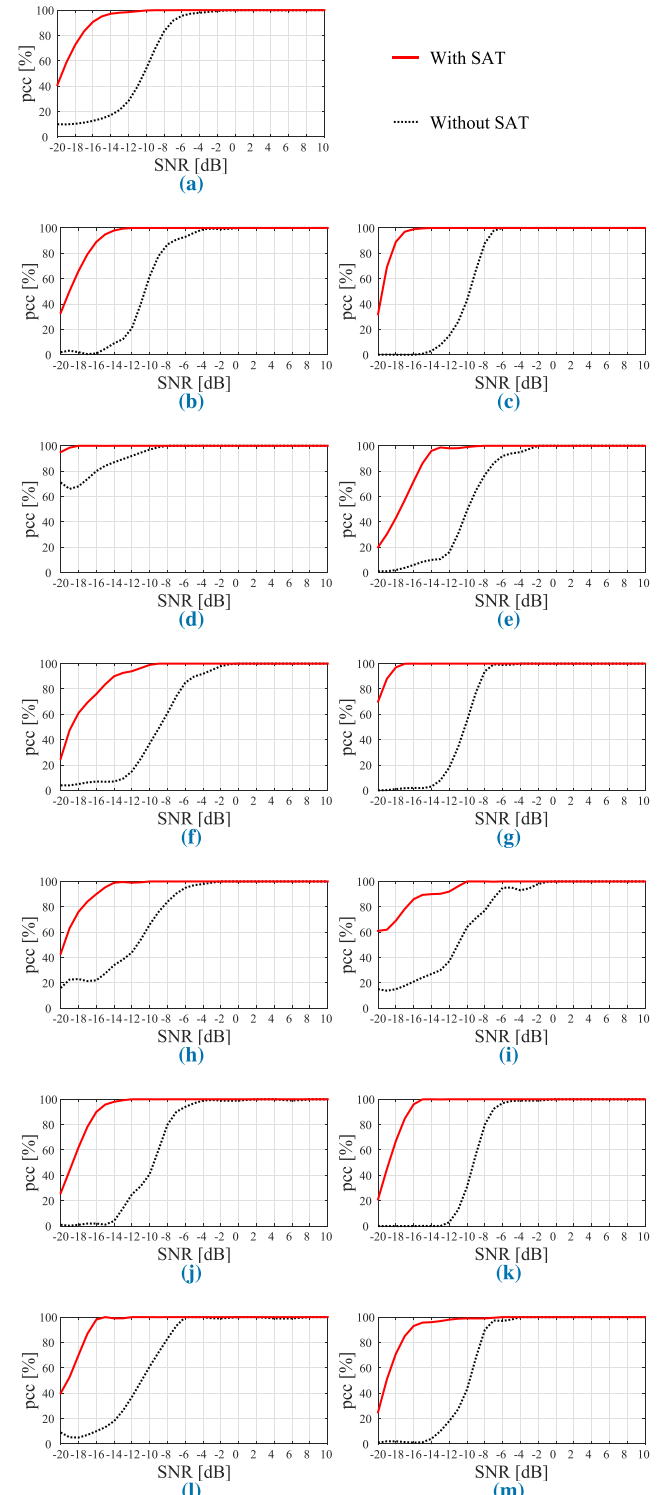
Table 4 defines the signal parameters and simulation conditions used for the performance evaluation of the proposed LWRT without the SAT, where f_c , B , N , f_{\min} , L_c , N_{cc} , M , ρ and N_g represent the center frequency, bandwidth of the intercepted signal, number of collected signal samples, fundamental frequency of the Costas code, code length, number of samples per cycle of the carrier frequency, number of frequency steps (or number of subcodes in one frequency step), number of the subcode in a code, and number of segments in a code, respectively. The parameter range in Table 4 is selected to satisfy the conditions such as $N_{sc} = 4$ and $N_s (= 2048) > N$ and to allow much wider variations of the signal than those in subsections V-A, V-B, and V-C. Notice that the bandwidth B_s of the receiver is assumed to be larger or equal to that of the LPI radar signal B and that the parameters related to the frequency and band-

TABLE 4. Signal parameters and simulation conditions.

Radar waveforms	Parameters	Value of Range
LFM	f_c	$U(f_s/6, f_s/5)$
	B	$U(f_s/20, f_s/16)$
	N	$U[512, 1920]$
Costas	FH sequence	{3, 4, 5, 6}
	f_{\min}	$U(f_s/30, f_s/24)$
	N	$U[512, 1920]$
BPSK	L_c	{7, 11, 13}
	f_c	$U(f_s/6, f_s/5)$
	N_{cc}	$U[20, 24]$
Frank , P1	f_c	$U(f_s/6, f_s/5)$
	N_{cc}	{3, 4, 5}
	M	{6, 7, 8}
P2	f_c	$U(f_s/6, f_s/5)$
	N_{cc}	{3, 4, 5}
	M	{6, 8}
P3, P4	f_c	$U(f_s/6, f_s/5)$
	N_{cc}	{3, 4, 5}
	ρ	{36, 49, 64}
T1, T2	f_c	$U(f_s/6, f_s/5)$
	N_g	{4, 5, 6}
	N	$U[512, 1920]$
T3, T4	f_c	$U(f_s/6, f_s/5)$
	B	$U(f_s/20, f_s/10)$
	N_g	{4, 5, 6}
	N	$U[512, 1920]$

width of the signal are expressed in terms of f_s . In addition, to avoid situations where the intercepted signals are easily classified with the difference between the center frequencies of the intercepted signals in the CWD-TFI, the center frequencies of the twelve waveforms are set to be the same.

For the training phase of the CNN in the proposed LWRT, we generate 2700 signals for each of the twelve waveforms with SNR ranging from -6dB to 10dB at a step of 2dB . Therefore, there are a total 32,400 signals generated, and we divide the training signal set into two groups: 70% (i.e., 22,680) for the training set and 30% (i.e., 9,720) for the validation set. The validation set, that is used to estimate the generalization error during the training phase, allows updating the hyper-parameters accordingly [28]. Then, 1600 test signals for each of the twelve LPI radar waveforms, with SNR ranging from -20dB to 10dB at a step of 2dB , are created to test the performance of the proposed LWRT. Therefore, there is a total 19,200 test data set generated to test the proposed LWRT. Note that we do not train the proposed LWRT by signals with SNR lower than -6dB since the CWD-TFIs becomes too noisy and they may confuse the system. Note also that we only use the signal set generated without using the SAT for the training phase.

**FIGURE 11.** Performance comparison of the proposed LWRT with and without the SAT for all of the twelve LPI radar waveforms in [2]. (a) Overall. (b) LFM. (c) BPSK. (d) Costas. (e) Frank. (f) P1. (g) P2. (h) P3. (i) P4. (j) T1. (k) T2. (l) T3. (m) T4.

In the tests of the proposed LWRT with the SAT, we generate signal samples at $N_a (= 10)$ times higher sampling frequency than f_s , and use the signal samples to test the

proposed LWRT with the SAT. For the proposed LWRT without the SAT, we down-sample the generated signal by N_a times to perform the test. We use $N_{sc} = 4$, and the simulation results shown in Fig. 11 testify that there is more than 9dB performance improvement by using the SAT with $N_a = 10$ and $N_{sc} = 4$. Note that slightly less than 10dB performance improvement is expected from the slight SNR loss due to the SAT. Notice that the computation complexities of the proposed LWRTs (with and without the SAT) are similar, and that the performance of the proposed LWRT without the SAT is slightly worse than the performance results shown in the previous subsections V-A, V-B, and V-C. This is because the proposed LWRT in this subsection is classifying all of the twelve waveforms, whereas, in the previous subsections, the proposed LWRT is required to classify only eight waveforms.

TABLE 5. Confusion matrix for $\text{SNR} = -6\text{dB}$.

	BPSK	Costas	LFM	Frank	P1	P2	P3	P4	T1	T2	T3	T4
BPSK	99	0	0	0	0	0	0	0	1	0	0	0
Costas	0	99	0	0	0	0	0	0	1	0	0	0
LFM	0	0	94	0	4	0	0	2	0	0	0	0
Frank	0	0	0	89	0	0	11	0	0	0	0	0
P1	0	0	2	1	86	0	0	10	0	0	0	1
P2	0	0	0	0	0	100	0	0	0	0	0	0
P3	0	0	1	7	0	0	91	1	0	0	0	0
P4	0	0	4	0	9	0	0	85	1	0	0	1
T1	1	0	0	0	0	0	0	0	97	0	2	0
T2	1	0	0	0	1	0	0	2	0	94	0	2
T3	0	0	0	0	0	0	3	0	1	0	95	1
T4	0	0	0	0	1	0	0	2	0	3	0	94

Table 5 shows the confusion matrix of the proposed LWRT without the SAT for $\text{SNR} = -6\text{dB}$. As shown, polyphase codes have low pcc, because the CWD-TFIs of the P1 and P4 codes can be confused with that of the LFM, and those of Frank and P3 codes can be confused, when the SNR is low.

VI. CONCLUSION

A CNN-based LPI radar signal classification technique has been proposed and tested for twelve intra-pulse modulated LPI radar waveforms introduced in the literature. The hyperparameters of the proposed technique has been determined to guarantee the maximum performance based on various simulations, and the proposed technique has demonstrated with numerous Monte Carlo simulations that it achieves a superior performance than the recent LWRTs introduced in the literature. In addition, it has been found that applying the SAT to the intercepted LPI signal samples can effectively reduce the number of signal samples to be processed by the intercept receiver and that the technique achieves a significant performance improvement without increasing the computation cost. Therefore, the proposed LWRT with and without

the SAT can be useful for LPI radar signal detection and classification in practice.

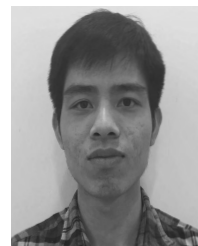
REFERENCES

- [1] R. G. Wiley, *ELINT: The Interception and Analysis of Radar Signals*. Norwood, MA, USA: Artech House, 2006.
- [2] P. E. Pace, *Detecting and Classifying Low Probability of Intercept Radar*. Norwood, MA, USA: Artech House, 2009.
- [3] G. López-Risueño, J. Grajal, and A. Sanz-Osorio, “Digital channelized receiver based on time-frequency analysis for signal interception,” *IEEE Trans. Aerosp. Electron. Syst.*, vol. 41, no. 3, pp. 879–898, Jul. 2005.
- [4] C. Wang, J. Wang, and X. Zhang, “Automatic radar waveform recognition based on time-frequency analysis and convolutional neural network,” in *Proc. IEEE Int. Conf. Acoust., Speech Signal Process. (ICASSP)*, Mar. 2017, pp. 2437–2441.
- [5] E. R. Zilberman and P. E. Pace, “Autonomous time-frequency morphological feature extraction algorithm for LPI radar modulation classification,” in *Proc. IEEE Int. Conf. Image Process.*, Oct. 2006, pp. 2321–2324.
- [6] M. Zhang, M. Diao, and L. Guo, “Convolutional neural networks for automatic cognitive radio waveform recognition,” *IEEE Access*, vol. 5, pp. 11074–11082, 2017.
- [7] J. Lunden and V. Koivunen, “Automatic radar waveform recognition,” *IEEE J. Sel. Topics Signal Process.*, vol. 1, no. 1, pp. 124–136, Jun. 2007.
- [8] M. Zhang, L. Liu, and M. Diao, “LPI radar waveform recognition based on time-frequency distribution,” *Sensors*, vol. 16, no. 10, p. 1682, 2016.
- [9] T. R. Kishore and K. D. Rao, “Automatic intrapulse modulation classification of advanced LPI radar waveforms,” *IEEE Trans. Aerosp. Electron. Syst.*, vol. 53, no. 2, pp. 901–914, Apr. 2017.
- [10] Y. Bengio, A. Courville, and P. Vincent, “Representation learning: A review and new perspectives,” *IEEE Trans. Pattern Anal. Mach. Intell.*, vol. 35, no. 8, pp. 1798–1828, Aug. 2013.
- [11] Y. LeCun, L. Bottou, Y. Bengio, and P. Haffner, “Gradient-based learning applied to document recognition,” *Proc. IEEE*, vol. 86, no. 11, pp. 2278–2324, Nov. 1998.
- [12] K. G. Sheela and S. N. Deepa, “Review on methods to fix number of hidden neurons in neural networks,” *Math. Problems Eng.*, vol. 2013, May 2013, Art. no. 425740, doi: [10.1155/2013/425740](https://doi.org/10.1155/2013/425740).
- [13] N. Levanon and E. Mozeson, *Radar Signals*. New York, NY, USA: Wiley, 2004.
- [14] M. I. Skolnik, “Introduction to radar,” in *Radar Handbook*, vol. 2. New York, NY, USA: McGraw-Hill, 1962.
- [15] J. A. Starzyk and Z. Zhu, “Averaging correlation for C/A code acquisition and tracking in frequency domain,” in *Proc. IEEE 44th Midwest Symp. Circuits Syst. (MWSCAS)*, vol. 2. Aug. 2001, pp. 905–908.
- [16] S.-H. Kong, “SDHT for fast detection of weak GNSS signals,” *IEEE J. Sel. Areas Commun.*, vol. 33, no. 11, pp. 2366–2378, Nov. 2015.
- [17] H.-I. Choi and W. J. Williams, “Improved time-frequency representation of multicomponent signals using exponential kernels,” *IEEE Trans. Acoust., Speech, Signal Process.*, vol. 37, no. 6, pp. 862–871, Jun. 1989.
- [18] P. Flandrin, “Some features of time-frequency representations of multicomponent signals,” in *Proc. IEEE Int. Conf. Acoust., Speech, Signal Process. (ICASSP)*, vol. 9. Mar. 1984, pp. 266–269.
- [19] J. E. Fielding, “Polytime coding as a means of pulse compression,” *IEEE Trans. Aerosp. Electron. Syst.*, vol. 35, no. 2, pp. 716–721, Apr. 1999.
- [20] J. A. Parker, R. V. Kenyon, and D. Troxel, “Comparison of interpolating methods for image resampling,” *IEEE Trans. Med. Imag.*, vol. MI-2, no. 1, pp. 31–39, Mar. 1983.
- [21] T. M. Lehmann, C. Gönnér, and K. Spitzer, “Survey: Interpolation methods in medical image processing,” *IEEE Trans. Med. Imag.*, vol. 18, no. 11, pp. 1049–1075, Nov. 1999.
- [22] Y. LeCun, K. Kavukcuoglu, and C. Farabet, “Convolutional networks and applications in vision,” in *Proc. IEEE Int. Symp. Circuits Syst. (ISCAS)*, May/Jun. 2010, pp. 253–256.
- [23] D. Ciregan, U. Meier, and J. Schmidhuber, “Multi-column deep neural networks for image classification,” in *Proc. IEEE Conf. Comput. Vis. Pattern Recognit. (CVPR)*, Jun. 2012, pp. 3642–3649.
- [24] P. Y. Simard *et al.*, “Best practices for convolutional neural networks applied to visual document analysis,” in *Proc. ICDAR*, vol. 3. 2003, pp. 958–962.

- [25] C. Poultney, S. Chopra, and Y. L. Cun, "Efficient learning of sparse representations with an energy-based model," in *Proc. Adv. Neural Inf. Process. Syst.*, 2007, pp. 1137–1144.
- [26] A. Krizhevsky, I. Sutskever, and G. E. Hinton, "ImageNet classification with deep convolutional neural networks," in *Proc. Adv. Neural Inf. Process. Syst.*, 2012, pp. 1097–1105.
- [27] N. Srivastava, G. Hinton, A. Krizhevsky, I. Sutskever, and R. Salakhutdinov, "Dropout: A simple way to prevent neural networks from overfitting," *J. Mach. Learn. Res.*, vol. 15, no. 1, pp. 1929–1958, 2014.
- [28] Y. LeCun, Y. Bengio, and G. Hinton, "Deep learning," *Nature*, vol. 521, pp. 436–444, May 2015.



MINJUN KIM received the B.S. degree in electronics engineering from Chung-Ang University, South Korea, in 2017. He is currently pursuing the M.S. degree with the CCS Graduate School of Green Transportation, Korea Advanced Institute of Science and Technology, South Korea. His research interests include signal processing, radar, deep learning, and V2X for autonomous vehicles.



LINH MANH HOANG received the B.S. degree in mechatronics engineering from the Hanoi University of Science and Technology, Vietnam, in 2012. He is currently pursuing the M.S. degree with the CCS Graduate School of Green Transportation, Korea Advanced Institute of Science and Technology, South Korea. His research interests include signal processing, radar, deep learning, and V2X for autonomous vehicles.



EUNHUI KIM received the B.S. degree in information communication engineering from Chung-Nam National University in 2000, and the M.Sc. degree in information communication engineering and the Ph.D. degree in electrical engineering from Korea Advanced Institute of Science and Technology (KAIST) in 2009 and 2015, respectively. She was an Assistant Engineer with the Visual Display Division, Software Team, Samsung Electronics, Suwon, South Korea, from 2000 to 2003, and an Associate Engineer with the Digital Solution Center, Architecture Team, Seoul, South Korea, from 2003 to 2007. She was a Post-Doctoral Researcher of computer science with KAIST from 2015 to 2016. Since 2017, she has been a Researcher with the CCS-Green Transportation Graduate School of Green Transportation. Her research interests include personalization in connected TV and auto vehicle, recommender systems, and big data processing with machine learning techniques.



SEUNG-HYUN KONG (M'06–SM'16) received the B.S. degree in electronics engineering from Sogang University, South Korea, in 1992, the M.S. degree in electrical engineering from Polytechnic University, Brooklyn, NY, USA, in 1994, and the Ph.D. degree in aeronautics and astronautics from Stanford University, Stanford, CA, USA, in 2006. From 1997 to 2004, he was with Samsung Electronics Inc., South Korea, and Nexpilot Inc., South Korea, where he was involved in the development of wireless communication system standards and UMTS mobile positioning technologies. In 2006, he joined Polaris Wireless Inc., Santa Clara, CA, USA, as a Staff Engineer, and from 2007 to 2009, he was with Qualcomm Inc. (Corporation Research and Development), San Diego, CA, USA, where his research focused on assisted-GNSS and wireless positioning technologies. Since 2010, he has been with the Korea Advanced Institute of Science and Technology, where he is currently an Associate Professor with the CCS Graduate School of Green Transportation. His research interests include signal processing for GNSS, neutral networks for sensing, and vehicular communication systems. He serves as an Editor for the *IET Radar, Sonar and Navigation* and an Associate Editor for the IEEE Transactions on Intelligent Transportation Systems and the IEEE Access.